npj | heritage science

Article

https://doi.org/10.1038/s40494-025-02279-5

Multi-analytical study of shaping firing and painted inscriptions in a Roman *Titulus Pictus* amphora

Martina Bernabale[1], Luca Buccini[1], Pierfrancesco Atanasio[1], Alessia Sanna[1], Anna Candida Felici[1,2], Daniele Passeri[1,3], Marco Rossi[1,3], Paolo Binaco[4] & Danilo Dini[3,5] ✉

During the Roman period, amphorae were essential for storing and transporting goods, especially food. This study examines a fragment of a Roman amphora with a red *titulus pictus*, discovered at the Poggio Moscini archaeological site (Bolsena, Italy) and dated between 150 and 100 BC. A comprehensive archaeometric study has been conducted using the non-disruptive techniques of X-ray microscopy (XRM), X-ray powder diffraction (XRPD), energy-dispersive X-ray fluorescence (ED-XRF) spectroscopy, fiber optics reflectance spectroscopy (FORS) and micro-Raman spectroscopy. XRM revealed a preferential pore orientation consistent with wheel-throwing manufacture. XRPD identified quartz, diopside, gehlenite, anorthite and sanidine, indicating the use of Ca-rich clays and firing temperatures between ~900 and 1000 °C. ED-XRF demonstrated a similar composition between the ceramic body and the pigment, confirming Fe-rich clay and Fe-oxide-based pigmentation. FORS shows absorption features typical of hematite, and micro-Raman spectroscopy identifies hematite as the red pigment and rules out gypsum in the ceramic body.

During the Roman period, amphorae were widely used for the storage and transportation of goods such oil and salted products, playing a critical role in the commercial network of the ancient Mediterranean[1]. One distinctive feature of many Roman amphorae is the presence of *tituli picti*—painted inscriptions in black or red ink on their external surfaces. These inscriptions are traditionally understood as a form of labeling, similar to what occurs also for the products of our present times, which provides key information about the dating, contents, origins, or destinations of the goods. The eventual standardization of this ancient practice of labeling across the Roman world suggests a complex commercial system with goods destined for increasingly specialized contexts. It has been recently proposed that these labels could have been linked with contracts of maritime insurance, which governed the rules of transport of goods, though this interpretation remains debated[2].

The present study focuses on a particular amphora fragment dated to the 2nd century on the basis of the shape/size analysis of the type of container and of the stratigraphical analysis of the ground portion surrounding the find spot[3]. The amphora fragment was discovered during the excavation campaigns of the French School in the archaeological area of Poggio Moscini near Bolsena (Viterbo), between 1962 and 1973. The artifact is currently exhibited at the Museo Territoriale del Lago di Bolsena[4]. The fragment of terracotta amphora bears a red inscription, or *titulus pictus* (Fig. 1), which can provide information about the economic, social and work practices of the time. The presence of a label like a *titulus pictus* on an ancient artifact renders particularly interesting the analysis of such an archaeological find and a preliminary study carried out with micro-Raman spectroscopy has revealed the presence of hematite, sienna earth, and rutile on the red inscription of the find in question[4]. Nevertheless, a more comprehensive characterization capable of differentiating the chemical-physical characteristics of the inner and exterior parts of the terracotta find is useful to clarify also the nature of the raw materials, the production techniques, and the operative conditions of manufacturing, like the firing temperatures[5–12]. For this purpose, a more comprehensive set of archaeometric techniques needs to be applied to further investigate the production processes and material composition of the amphora bearing the red *titulus pictus*[13]. The techniques of characterization employed in this study include X-ray microscopy (XRM), X-ray powder diffraction (XRPD), energy-dispersive X-ray fluorescence spectroscopy (ED-XRF), fiber-optics reflectance spectroscopy (FORS) and micro-Raman spectroscopy. The combined use of these methods provides complementary information on the artifact's chemical and structural composition. In particular, XRM, a non-destructive

---

[1]Department of Basic and Applied Sciences for Engineering (SBAI), Sapienza University of Rome, Rome, Italy. [2]Research Center for Applied Sciences to the Safeguard of Environment and Cultural Heritage (CIABC), Sapienza University of Rome, Rome, Italy. [3]Centro di Ricerca per le Nanotecnologie Applicate all'Ingegneria della Sapienza (CNIS), Sapienza University of Rome, Rome, Italy. [4]Museo Territoriale del Lago di Bolsena, Bolsena, VT, Italy. [5]Department of Chemistry, Sapienza University of Rome, Rome, Italy. ✉e-mail: danilo.dini@uniroma1.it

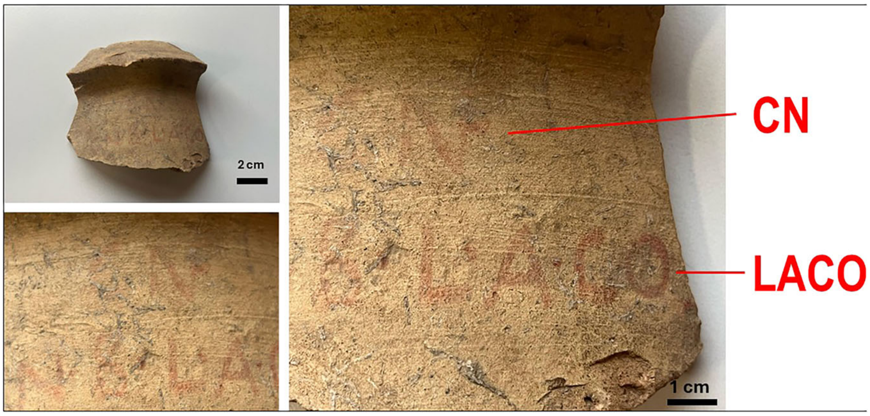

Fig. 1 | Various images of the amphora fragment with *titulus pictus*. The details of the red inscriptions are evidenced.

imaging technique, is employed to analyze the internal structure of the fragment. Such an instrumentation can offer a glimpse on the manufacturing techniques of the time and eventually verify the existence of internal repairs or modifications not appearing to the bare eye[14–16]. It is here anticipated that XRM resulted particularly valuable for investigating the presence, morphology, and orientation of structural discontinuities, as well as coil-joins, variations in wall thickness, surfaces rolling marks and finger impressions on not cooked, soft fragments: these potentialities of XRM enable a detailed reconstruction of the adopted techniques of forming[17] thanks to the capability of detecting subtle contrasts of density in finds with stratified features in their inner parts and, even more clearly, between the solid clay components and the voids[8]. Compared to the mineralogical and petrographic approaches that make use of thin sections of samples (with consequent limitations in sizes for non-destructible samples), XRM allows the in-depth visualization of the overall morphological characteristics of the object[18–20]. X-ray imaging allows for the examination of large areas, creating virtual cross-sections through the samples in three dimensions without disrupting the sample. However, the sole XRM technique does not provide information about the chemical composition of a solid sample[21–25], and its use needs to be complemented by the use of a technique like ED-XRF that allows the non-destructive elemental analysis of an object surface for the identification of the chemical elements present in the inscription and the underlying terracotta[26]. Lastly, micro-Raman spectroscopy and XRPD will offer detailed information, respectively, on the chemical species present on the surface and on the crystalline phases of the materials that constitute the *titulus pictus* find. The combined analysis of the results from micro-Raman and XRPD techniques will provide information that is essential for identifying unambiguously the mineral components of the amphora's fabric and the pigments used for the realization of the inscription[11,12,27].

The advanced scientific analysis obtained using the multi-techniques approach here considered aims at the understanding of the amphora's production methods, and at the determination of the nature of the materials present in the various phases of amphora construction, processing (drying/cooking) and decoration. Such an investigative effort is directed toward the attempt to clarify the significance of this specific artifact within the broader framework of ancient Mediterranean trade, taking advantage of the historical context and the archaeological data, which are relevant to the period during which the *titulus pictus* amphora was manufactured and used.

Methods

The sample is a Roman amphora fragment with a red *titulus pictus* (Fig. 1), and it consists of partially preserved inscriptions that likely indicated in *totum* the producer, contents, or recipient of the amphora. Despite surface wear, some letters of the *titulus* are readable especially in the lower section, where more clearly appears the sequence "LACO", which might refer to the name of a producer, merchant or other (*vide infra*). The upper row of the remaining text appears faded, but initial analysis suggests it is a name abbreviation. The red text of the *titulus pictus* is quite clearly readable with characters having a height of 3.7 cm, and it is distributed along two rows:

first row: **CN** [---]
second row: **CN** · **8** · **L** · **A** · **CO()**[28]

Some marks of punctuation are present. The letters CN that are present in the first row and at the beginning of the second row probably represent abbreviations of the *praenomen* (first name) *Cnaeus*. Regarding the sign in the shape of an "8," there is some uncertainty about the interpretation of this specific mark made by the first editor who reported the find. According to that interpretation, the "8" could represent the Etruscan letter F[29], thereby supporting the hypothesis that the text was inscribed on an amphora intended for use within a regional context. The letter could be the abbreviation of "*filius*" (= son) and the resulting interpretation would be

CN (aeus)
CN (aei) · **f(ilius)** · **L()** · **A ()** · **CO ()**[30]

According to this hypothesis, there is the recognition of the coexistence of the Etruscan and Latin alphabets in the same vase, a fact that would denote the simultaneous use of both alphabets at that time. The simultaneous use of the Etruscan and Latin alphabets, both being already well distinct, has been previously documented in the territory of *Volsinii* (the actual Bolsena). The references are a series of finds dated in the 2nd BC century with the letters that have been engraved onto a Greek-Italic amphora[31]. Alternatively, the graphic mark "8", could be an approximate version of the Latin graphic mark B to abbreviate the name of a noble person. For this latter interpretation it is helpful to examine also the letters of the second part of the second row in which appear the letters "L", "C", "A" and "O" which are also interpreted as abbreviations. "L" would stand as initial of the first name "*Lucius*" whereas "CO" could be the abbreviation of a noble name or that of the word consul ("*CO(n)S(ule)/CO(n)S(ulibus)*"). A very tiny red drawing, found in correspondence with the amphora break, could be referred to the tail of an "S" which disappeared with the rest of the amphora. In this case the most accredited hypothesis of interpretation is

$$CN(aeus)[---]/CN(aei)\,B()\,L()\,A()\,CO[---]$$

or alternatively

CN(aeus) [---] / CN(aei) B() L() A() CO(n)Ṣ(ule)

In this case, it would appear very helpful and suggestive the comparison between the *titulus pictus* under consideration and the other one, reported on a Greek-Italic amphora that was found in Capena (Rome, Italy). The text reported in the amphora of Capena (not shown) is interpreted in two similar manners[32]:

$$Gn.Etrili/L\cdot\ Ani(cio)\ \cdot\ co(n)s(ule)/F(alernum)$$

Table 1 | Parameters of XRM scans

Pixel size	34 µm
Voltage	80 kV
#Projections	1600
Exposure time	8 s
Acquisition Mode	Wide Field

or alternatively[33]

$$Cn.Etril(i)/L \cdot\ Ani(cio)\ \cdot\ co(n)s(ule)/F(alernum)$$

Similar to the *titulus pictus* of *Volsinii*, the text from Capena is written with red pigments and thanks to the identification of the consul governing at the time of the production/use of the amphora the latter could be dated at about 160 BC[34]. In addition to already mentioned *Lucius Anicius Gallus*, the other consuls operating during 2nd century BC with the first name starting with "A" were *Lucius Aurelius Orestes* I (157 BC), *Lucius Aurelius Cotta* (144 BC), *Lucius Aurelius Orestes* II (126 BC), *Lucius Aurelius Cotta* II (119 BC) and *Lucius Aurelius Orestes* III (103 BC). For the Roman region of *Volsinii* and the surrounding area of southern internal Etruria region, the dating of the amphorae within the range 160–100 BC is made possible through the name of the governing consul with a red *titulus pictus*. This would confirm the dating of the amphora (Fig. 1) within the broader temporal range 200–100 BC.

X-ray microscopy

XRM experiments were performed using a ZEISS Xradia Versa 610 (Carl Zeiss X-ray microscopy, Dublin, CA, USA) available at the Research Center on Nanotechnology Applied to Engineering of Sapienza University of Rome (CNIS). The XRM is part of the Open Infrastructure for Advanced TOmography and Microscopies (ATOM). XRM parameters are reported in Table 1. The figures have been created with Dragonfly 3D World 2024.1 Built 1627.

X-ray powder diffraction

XRPD analysis was carried out with a Rigaku Miniflex diffractometer at the Cu-Kα radiation wavelength of 1.54 Å in the 2θ range of 10–60°, with operative electrical parameters 30 kV and 15 mA, respectively, for the voltage and for the current. This technique requires the withdrawal of a few milligrams ofthe sample in the form of powder. The measurements were performed on two distinct areas of the *titulus pictus*: one closer to the surface and another from a more internal region. A small amount of powder was carefully scraped from the fracture zone, without causing any aesthetic damage to the object. This method aims to distinguish eventual structural/compositional differences between the outermost layers and the inner parts of the material. The approach helps in providing information about possible variations in crystalline phases due to cooking techniques that have been used in the production of the amphorae and/or due to degradation phenomena that occurred with time.

Energy-dispersive X-ray fluorescence

Elemental analysis was performed using an ED-XRF spectrometer equipped with an X-ray tube (Amptek Mini-X, Amptek Inc., Bedford, UK) with a rhodium anode target and a 127 µm thick beryllium window. The tube operated at an accelerating voltage of 40 kV and an electronic current of 80 µA. Detection was carried out using a Peltier-cooled silicon drift detector (Amptek 123-SDD) with an integrated amplifier and multichannel analyzer, which generates a current pulse proportional to the energy of each detected X-ray photon. The area sampled by the spectrometer was about 14 mm^2 and the acquisition time was 300 s. ED-XRF spectra were processed using PyMCA 5.9.2. Elemental results are reported as relative peak intensities (counts), providing semi-quantitative information suitable for comparing signal variations across analyzed areas[35].

Fiber optics reflectance spectroscopy

Fiber optics reflectance spectroscopy was performed with an AvaSpec spectrophotometer (Avantes, Apeldoorn, The Netherlands) equipped with a CCD linear sensor (2048 pixels) and a diffraction grating with 300 lines/mm, blazed at 500 nm, which covers a spectral range from 300 to 1100 nm at the spectral resolution of 0.8 nm. The light source was a halogen lamp (HL-2000 FHSA, Avantes). The measurement geometry was 2 × 45°:0° through a bifurcated fiber (diameter of 600 µm) for the illumination and a 200 µm diameter fiber (NA 0.22 ± 0.02) for the collection of the reflected light. The sampled area diameter is 1 mm. The system uses the Avantes software AvaSoft-COL. The reflectance spectra were collected from 380 to 1000 nm with an integration time of 70 ms and an averaging of 100 scans. A portable digital microscope (AM7915MZT-Edge, Dino-lite, Almere, The Netherlands) was employed to acquire the images.

Micro-Raman spectroscopy

Micro-Raman analyses were conducted at room temperature with an inVia™ confocal Raman spectrometer (Renishaw) having a 250 mm focal length. The system featured an 1800 l/mm holographic diffraction grating and a Peltier-cooled CCD detector. A continuous-wave Nd diode-pumped solid-state laser (Renishaw) with a 532.1 nm wavelength (green laser) and 50 mW output power served as the excitation source. The laser beam was focused on the samples with a 50× short working-distance N-Plan objective (N.A. = 0.75, Leica Microsystems). For mapping, a dataset of 200 points was acquired with a 50× objective lens having a spatial resolution of 1 µm and a step size of 2 µm between adjacent points. Measurements were performed at 10% of laser power, with exposure time of 1 second and ten accumulations per point at 1020 cm^{-1} as central wavelength of signal acquisition.

Results

X-ray microscopy investigation

The XRM virtual slices presented in Fig. 2a-c illustrate the microstructure of the *titulus pictus*, respectively, along the YZ, XZ, and XY planes defined by three arbitrary orthogonal axes. The analysis provides a sectional view of the fabric's texture and reveals inclusions and porosity for the matrix. The matrix, in grey scale color, appears fine and compact with a homogeneous distribution of mineral inclusions and pores. Inclusions, mostly visible as bright particles, are primarily sub-angular to rounded, with some irregular shapes. The variability in grey scale levels reflects differences in X-ray absorption coefficients and/or thickness within the sample. Pores are relatively evenly distributed and exhibit irregular morphologies, ranging from elongated to rounded forms.

Their size varies, with smaller pores dispersed throughout the matrix and larger, well-defined voids. This porosity likely results from the paste composition, manufacturing techniques, and firing conditions, which influenced the material's sintering behavior. The virtual cross-sections and 3D rendering of the object reveal a distinct outer layer of the artifact with a different, relatively higher density (Fig. 3a, b). The outer layer displays a thickness ranging from approximately 1.8 mm to 2.8 mm, as marked in the image. This layer appears darker compared to the interior of the fragment. This contrast difference suggests a possible variation in density or composition between the core and the surface, which could be related to thermal or mechanical processes during shaping and firing. Another explanation could be the mechanical compaction during the shaping process.

X-ray microscopy has also been employed to identify primary forming methods, such as pinching, drawing, coil-building, slab-building, moulding and wheel-throwing, since the application of pressure to plastic clay causes mineral particles, voids and organic fragments to take up a preferred orientation with the resulting redistribution affecting the whole clay body. It is well known that resulting alignment and distribution of inclusions and voids are characteristic of each forming method and will not normally be obliterated by secondary forming or decoration procedures[36].

In Fig. 4a the voids have been segmented in red and treated as individual objects that can be characterized by the *basic measurements tools* available for 3D multi-ROIs (Fig. 4b).

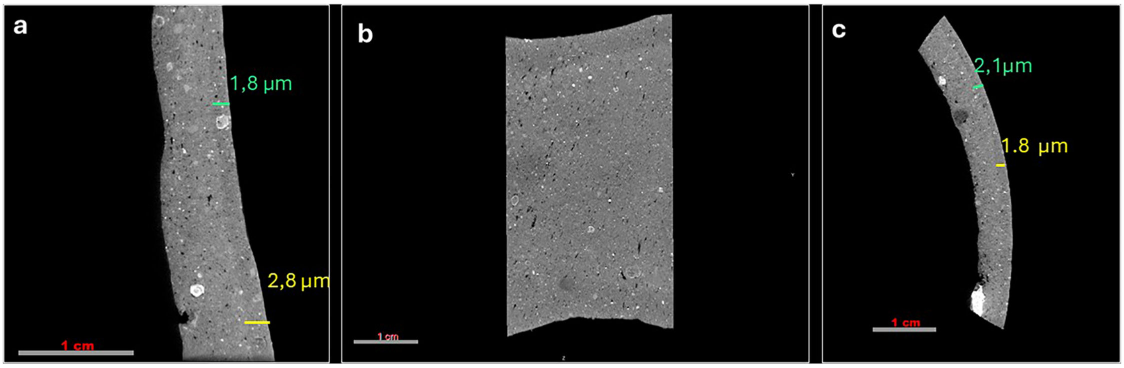

Fig. 2 | X-ray microscopy (XRM) pictures of the terracotta fragment from different sides of view. XRM pictures of virtual slices along the YZ (**a**), XY (**b**), and XZ (**c**) planes chosen according to an arbitrary set of three orthogonal axes. The three representations show the microstructure of the amphora fragment. The greyscale intensity represents material density: darker areas correspond to pores and voids (lower density), while brighter regions indicate denser inclusions. The measured thicknesses of different regions are annotated.

Fig. 3 | 3D rendering of the amphora fragment obtained through X-ray Microscopy (XRM). The cubic insets in the figures indicate the orientation of the axes of visualization with respect to the sample. The arrow in (**a**) highlights the presence of a denser outer layer, possibly due to thermal or mechanical processes. Image (**b**) shows 3D structure with visible inclusions. Density variations within the fragment are distinguishable based on color intensity.

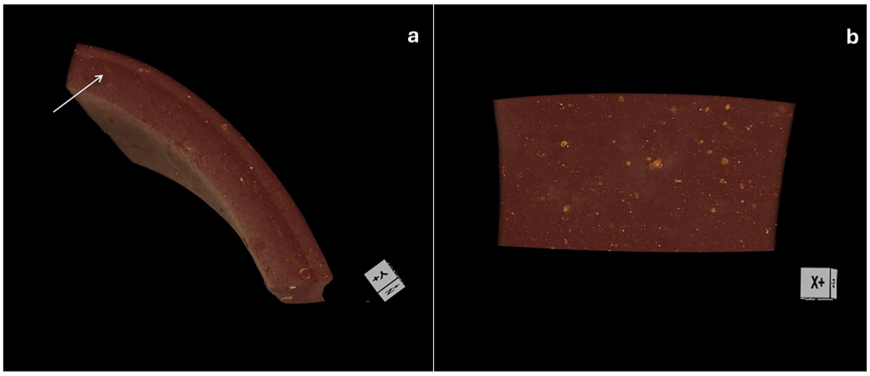

Here, the voids in the amphora fragment have been segmented and analyzed based on their orientation and measured using the Phi (°) angle. The Phi angle is equal to the rotation of the X-Y plane towards the Z-axis. From the color scale, a predominance of blue and green voids can be observed: this denotes a preferential alignment along the chosen Z-axis and suggests a compression and a stretching effect typical of wheel-throwing[21,23,37]. This is because, during wheel-forming, the centrifugal force applied to the clay causes the voids to align perpendicularly to the expanding surface. The red and orange voids, corresponding to higher Phi values, indicate a stronger inclination towards the X-Y plane and are less present than the blue and green ones. This distribution of voids is consistent with a wheel-throwing process rather than other techniques such as coil-building or hand modeling, which, in turn, would typically generate voids with more random orientations or inclinations along multiple directions, without alignment to a clear preferential direction.

In Fig. 5a, the voids in the amphora fragment have been extracted and visualized as three-dimensional meshes to observe the distribution of their morphology. The color map represents the Gaussian curvature of the internal surfaces: this measure describes the local geometry at a point on the surface and can take positive values (indicative of closed surfaces like a sphere) or negative values (indicative of saddle-shaped surfaces like the case of a hyperboloid) (Fig. 5b). The results show that larger and more elongated voids along the Z-axis tend to have regions with lower or even negative Gaussian curvature (represented in blue and light blue): these determinations indicate the presence of more cylindrical or saddle-like surfaces. This finding can be attributed to the pressure applied during shaping, which deforms the voids by stretching them along a preferred direction. In contrast, smaller, more isolated, and rounded pores exhibit predominantly positive Gaussian curvature (in yellow and orange in Fig. 5b), typical of closed, non-elongated cavities. This distribution is clearly consistent with a wheel-throwing manufacturing process, where the pressure exerted during shaping influences the orientation and the type of deformation of the voids. Figure 5c shows 3D rendering of a selected area of *titulus pictus* with segmented voids (in red) and inclusions (in turquoise).

X-ray powder diffraction analysis

XRPD analysis was conducted on powdered samples taken from both the inner and outer surfaces of the ceramic fragments. Figure 6 presents two distinct diffractograms, each representing the mineralogical composition of the corresponding surface in the artifact. The inner surface diffractogram identified quartz, diopside, gehlenite, hematite, plagioclase, and sanidine, whereas the outer surface exhibited a different mineral assemblage that includes quartz, sanidine, plagioclase, gehlenite and diopside. The absence of calcite suggests that the ceramic was fired at temperatures exceeding 950 °C, at which the complete decomposition of calcite occurs (thermal decarbonation). The formation of gehlenite results from high-temperature reactions between silica (SiO_2), alumina (Al_2O_3), and the calcium oxide (CaO) that is formed after decarbonation of calcite ($CaCO_3$) in accordance with the reaction:

$$Al_2O_3 + SiO_2 + 2CaCO_3 \rightarrow Ca_2Al_2SiO_7 + 2CO_2$$

The latter chemical process consists of the thermal breakdown of clay and carbonate minerals. This reaction occurs during the decarbonation

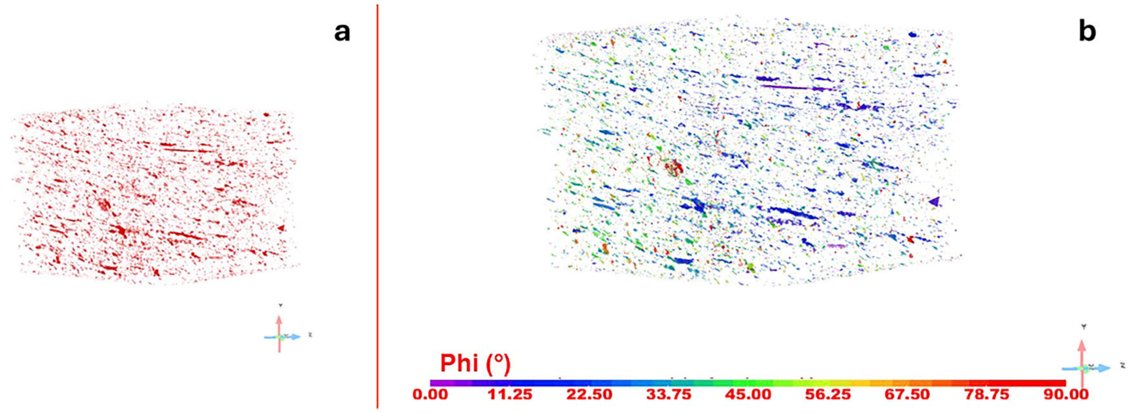

Fig. 4 | XRM visualization of the voids present in the inner parts of the terracotta fragment. Voids characterization by XRM: **a** segmented voids in red, **b** color map based on the angle inclination (phi) of the voids. Data illustrate a preferential alignment along one axis (the Z-axis), and it is indicative of a wheel-throwing shaping technique.

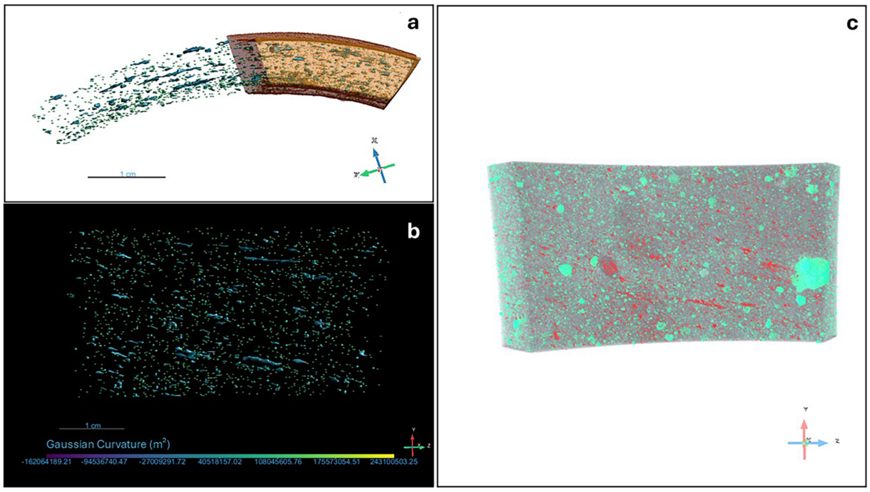

Fig. 5 | XRM visualization of the voids present in the inner parts of the terracotta fragment after application of a predefined curvature. a, **b** XRM meshes of voids according to Gaussian curvature. **c** 3D rendering of a selected area of titulus pictus with segmented voids (in red) and inclusions (in turquoise).

process, with experimental data indicating that gehlenite remains stable between 850–950 °C[38,39].

At temperatures above 800 °C, interactions between carbonate and silicate phases lead to the formation of sanidine and anorthite, according to the reaction[40]:

$$\mathrm{KAl_2(Si_3,Al)O_{10}(OH)_2 + CaCO_3 + 2SiO_2} \\ \rightarrow \mathrm{KAlSi_3O_8 + CaAl_2Si_2O_8 + CO_2 + H_2O}$$

Diopside ($CaMgSi_2O_6$) formation occurs at high temperatures, typically above 900 °C, through the reaction between quartz and dolomite [$CaMg(CO_3)_2$][5]:

$$\mathrm{2SiO_2 + CaMg(CO_3)_2 \rightarrow CaMgSi_2O_6 + 2CO_2}$$

This phase remains stable at temperatures exceeding 1200 °C and is commonly found in high-fired ceramics. The presence of diopside in terracotta matrix suggests that the firing conditions reached at least 900–1000 °C, further supporting the evidence from the absence of calcite and the presence of gehlenite.

Regarding iron oxide formation, hematite develops under oxidizing conditions at temperatures exceeding 600 °C, as shown by the reaction:

$$\mathrm{2\alpha FeOOH \rightarrow \alpha Fe_2O_3 + H_2O}$$

The fact that hematite was detected primarily in the inner portion and not on the outer surface is due to the sampling procedure, which avoided the areas near the red inscriptions to prevent damage to the artifact. However, part of this mineral is also present within the terracotta matrix.

Chemical analysis by ED-XRF

The ED-XRF analysis of the amphora's surface (Fig. 7) revealed no significant differences in elemental composition between the red inscriptions ("C", "L", "O") and the ceramic body (points 1 and 2 on unpainted substrate, fractures, back). This result is consistent with the XRPD data, which identified Ca-rich mineralogical phases in the ceramic. The high Ca content observed across all measurement points, therefore, reflects the use of a Ca-rich raw clay in the manufacture of the amphora. In this mineralogical context, the presence of Sr is expected, as Sr commonly substitutes Ca in Ca-bearing phases such as calcite, diopside, and plagioclase.

Among the inscription samples, "L" shows the highest Fe intensity, closely followed by fracture 2. A positive correlation between Fe and Ti is evident across the dataset and is consistent with the presence of ilmenite-type phases. Titanium is also compatible with the occurrence of anatase or rutile, oxides typically associated with the finer clay fraction in ceramic bodies[3].

The association of Ca and S may indicate the presence of gypsum ($CaSO_4{\cdot}2H_2O$), although this phase could also result from surface precipitation or post-depositional processes. The detection of Sr, on the other hand, is plausibly related to its substitution for Ca within calcium-rich mineral phases or to the presence of celestine ($SrSO_4$). This interpretation

Fig. 6 | X-ray Powder diffraction (XRPD) analysis of the terracotta fragment. XRPD patterns of **a** the outer surfaces and **b** of the inner part of the pottery fragment. The main mineralogical phases identified in the diffractograms are indicated.

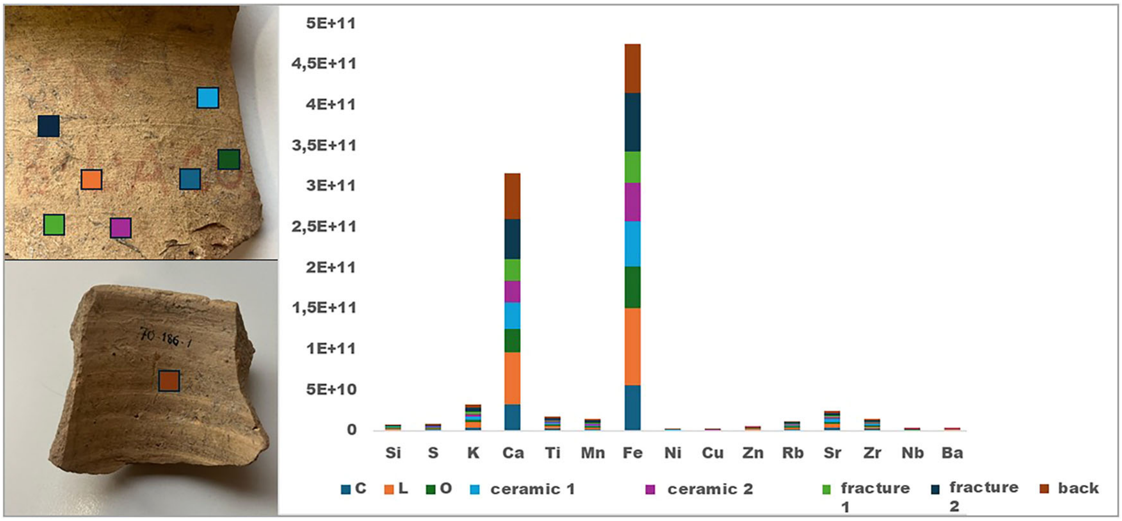

Fig. 7 | Analysis of the terracotta fragment with ED-XRF. Relative elemental composition of *titulus pictus*' surface as obtained by ED-XRF spectroscopy at the different points indicated on the terracotta pictures on the left side of the figure.

will be further assessed through the integration of Raman spectroscopy data. These results confirm the presence of iron-based compounds in both the red pigment used for the inscriptions and the ceramic substrate and highlight the need for additional analytical techniques to further investigate the mineralogical composition of the clay and pigments (vide infra). The ED-XRF spectra and counts are shown in Supplementary Data.

FORS analysis

The FORS analysis was specifically conducted on the red *titulus pictus* inscription (letters "A", "C", "L") visible on the surface of the amphora. The analysis revealed distinct spectral characteristics indicative of the pigment used. The reflectance spectra of the inscriptions exhibit a characteristic S-shape between 550 and 600 nm, a typical feature of hematite (Fe_2O_3). A pronounced absorption in the blue-green region (400–500 nm) is observed together with a gradual increase in reflectance towards the red and near-infrared regions (Fig. 8a). In highly absorbing, non-transparent samples, the absorbance, A, is inversely proportional to the reflectance, R, and it holds the relationship $A = \log(1/R)$][3]. The reflectance signal stabilized beyond 700 nm (Fig. 8a). Despite the spectra of the terracotta surface (points 1, 2, 3) are similar to those of inscription, they exhibit greater variability, likely due to intrinsic differences of the substrate material. In addition, the spectrum of terracotta in point 3 (black curve) shows a lower overall reflectance.

The first derivative analysis further supports these results (Fig. 8b). The inscriptions show a maximum derivative peak between 575 and 580 nm, a datum corresponding to the inflection point of hematite reflectance (red curves)[41]. On the other hand, the terracotta surface spectra (black curves in Fig. 8a,b), exhibit weaker derivative signals, and highlight a difference between inscriptions and bare substrate surface.

The microphotographs captured with the Dino-Lite digital microscope reveal additional details of the *titulus pictus* surface. In images of Fig. 8A–C, prominent white and dark veins are visible across, likely corresponding to mineral inclusions, secondary deposits from burial conditions or residues from restoration interventions, such as consolidants or protective treatments carried out after excavation. In contrast, the images of Fig. 8D,E focus on the areas near the red inscriptions, where distinct variations in texture and color can be observed. Some sections appear faded or eroded, suggesting potential post-burial alterations or mechanical wear.

Micro-Raman spectroscopy analysis

The micro-Raman spectroscopic analyses conducted on the Roman amphora revealed the composition and distribution of mineralogical

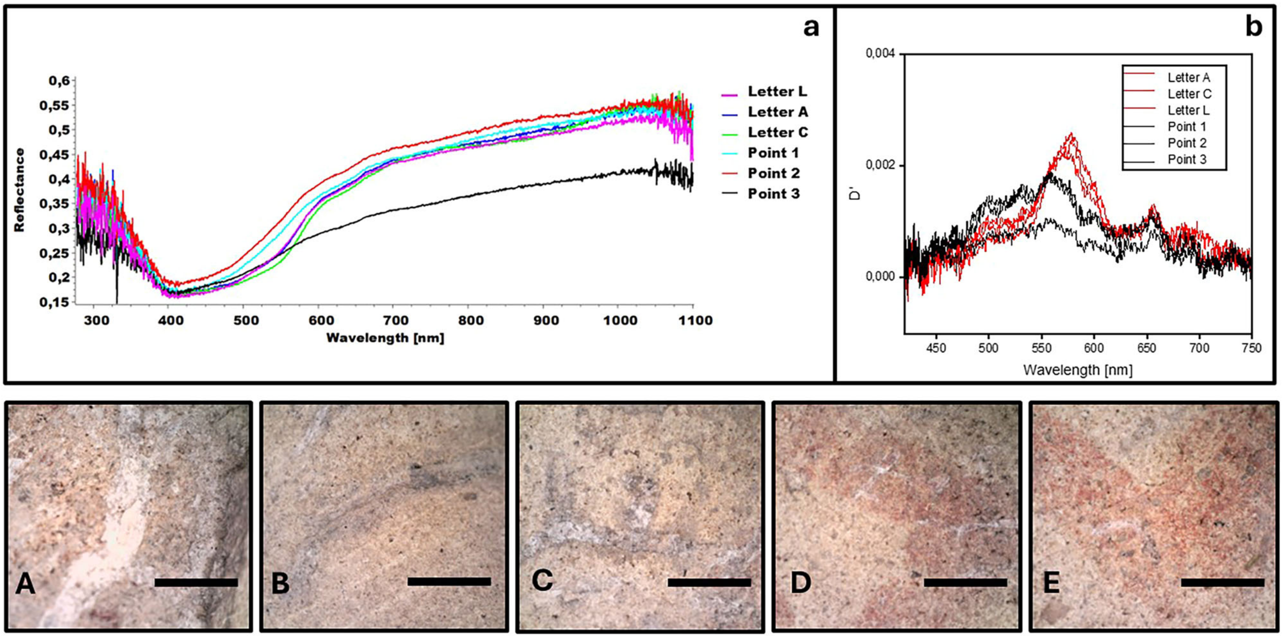

Fig. 8 | Reflectance spectra of the terracotta fragment obtained with the Fiber Optics Reflectance Spectroscopy (FORS) technique. **a** FORS spectra of the red-painted inscription and terracotta surface and **b** first derivative of the corresponding FORS spectra. A,B,C,D and E are the microphotographies of the amphorae's surface recorded at different points. Horizontal scale bar: 2 mm.

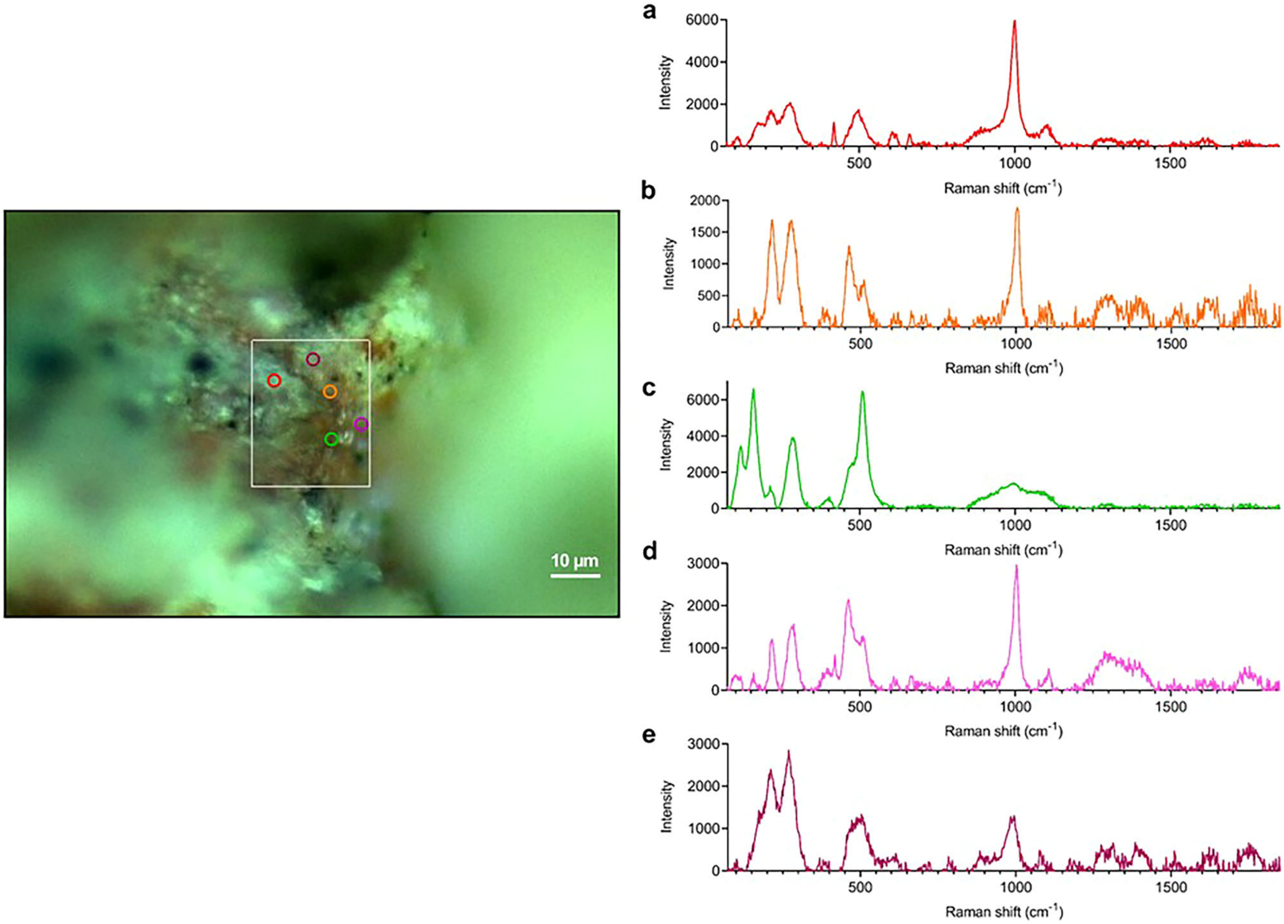

Fig. 9 | Micro-Raman spectra of a microscopic portion of titulus pictus, which includes the bare substrate and the zone with the red inscription. Raman data confirm the presence of hematite, sanidine, and gypsum on the surface. The color of the spectral profiles in **a**-**e** refers to the spectra of the areas indicated by the circles of the same color.

phases: the available data suggest a mixture of various phases both on the terracotta surface and the red inscriptions, in different proportions. To better discriminate the contribution of the mineralogical species constituting the inscription from those of the surrounding ceramic surface, a Raman map was generated, and the most representative spectra of the obtained data are shown (Fig. 9).

Overall, the spectra of the bare substrate and the red inscription show similar peaks, with slight variations in intensity and frequency shifts. The main peaks that have been identified include those characteristics of sanidine at 157, 211, 282, 403, 511, 995 cm^{-1} (Fig. 9c). Sanidine is a high-temperature polymorph of K-feldspar that forms above 850 °C and remains stable up to at least 1200 °C. In ceramic firing, K-feldspars can undergo transformations depending on the temperature and overall composition of the system. At temperatures exceeding 850 °C, microcline (or orthoclase) may transform into sanidine, while at even higher temperatures, interactions with lime can lead to the formation of anorthite[5].

The Raman data, together with the mineralogical information obtained by XRPD, suggest that the raw clay used for the amphora was illite-rich and contained K-feldspar. Illite generally begins to decompose above ~950 °C, and the observed transition from microcline-type feldspar to sanidine is consistent with firing conditions within this range[5].

The peaks recorded at 418, 497, 608, 628, 661, and 999 cm^{-1} are characteristic of gypsum ($CaSO_4{\cdot}2H_2O$) (Fig. 9a, b, d, e). The diffuse presence of gypsum suggests that it may have originated from various factors. Its presence within the terracotta matrix could indicate that the primary phase was probably anhydrite (anhydrous $CaSO_4$), maybe originating from local evaporite deposits. During post-firing processes, the anhydrite may have undergone hydration, forming gypsum[27]. Furthermore, the thin layer of gypsum frequently observed on the surface of the samples could be attributed to the percolation of sulphate-rich fluids in the burial environment[27]. In addition to that, some of the gypsum detected could be associated with restoration interventions, where it was potentially used as a filling or consolidation material, or applied as a protective coating for conservation purposes. Another significant finding was the identification of hematite (Fe_2O_3) through the recording of the peaks at 218, 279, 605, 660, and 1301 cm^{-1}. Such a determination indicates the presence of this red iron oxide both in the red inscriptions and the ceramic matrix (Fig. 9a, b, d, e). This is common in Roman manufactures since hematite was often used as a red pigment. Hematite starts to crystallize above 600 °C, and its presence indicates an oxidizing atmosphere[38,42].

No substantial differences were observed between the red inscriptions and the ceramic surface, suggesting a similar composition.

Discussion

The archaeometric investigation of the amphora fragment with non-invasive techniques has provided significant insights into both the production process of pottery in terracotta and the materials used for the painted inscription. One of the most significant aspects of this research is the analysis of the high-temperature firing process through the determination of the phases of diopside, gehlenite, anorthite, sanidine, and hematite within the terracotta matrix. The combination of non-invasive and minimally destructive analytical techniques, such as XRM, XRPD, ED-XRF, FORS, and micro-Raman spectroscopy[43], allowed for a comprehensive characterization of the artifact without the need to prepare thin sections, i.e. without dissecting the sample. These methods provided detailed information on the mineralogical, chemical, and microstructural properties of both the terracotta matrix and the overlying inscription.

The identification of diopside ($CaMgSi_2O_6$) and gehlenite ($Ca_2Al_2SiO_7$) suggests that the firing temperature ranged between 850 °C and 950 °C, as these minerals typically form through solid-state reactions between clay minerals and calcium carbonate at elevated temperatures. The absence of calcite further supports the hypothesis that the raw clay was fired above 950 °C, i.e., a temperature range at which CO_2 is expelled from carbonates thus leading to calcite complete thermal decomposition.

Although elemental analysis with ED-XRF detected high calcium concentrations on the terracotta surface, neither Raman spectroscopy nor XRPD could detect calcite suggesting that the original carbonate content underwent full decarbonation. This process likely facilitated the neo-formation of gehlenite, a characteristic transformation occurring at high temperatures.

The presence of anorthite ($CaAl_2Si_2O_8$) and sanidine (K-feldspar, $KAlSi_3O_8$) provides additional insights into the thermal history of the terracotta pottery fragment. Anorthite formation occurs at temperatures above 950 °C, through reactions between aluminosilicates and calcium, a finding that supports the hypothesis that the firing temperature exceeded this threshold. Meanwhile, the detection of sanidine, the high-temperature polymorph of K-feldspar, suggests that the terracotta was exposed to temperatures approaching or exceeding 1000 °C, as sanidine crystallizes preferentially at high temperatures with respect to orthoclase (or microcline).

The coexistence of diopside, gehlenite, anorthite, and sanidine indicates a firing temperature likely in the range of 950–1050 °C, where calcite decomposition, feldspar transformation, and pyroxene formation occur concomitantly.

Another observation in this study is the widespread presence of hematite (Fe_2O_3) in both the terracotta matrix and the painted inscription. The Raman spectra and FORS data confirm that the red pigment consists predominantly of hematite, a common iron oxide used in Roman manufacture for coloration. However, the fact that hematite is also present within the terracotta body suggests that iron-rich clays were originally used in the fabrication of the amphora. The consistency of hematite detection across all techniques confirms its role as the primary pigment.

X-ray microtomography provided valuable evidence regarding the forming technique of the amphora. The segmentation and analysis of voids within the ceramic matrix revealed a predominant alignment along a preferential axis, a feature characteristic of wheel-thrown pottery. This pattern results from the centrifugal force applied during shaping, causing the voids to stretch perpendicular to the expanding surface. Unlike completely hand-built artifacts, where voids exhibit more random orientations, the void distribution in this fragment aligns with known Roman wheel-throwing techniques.

Data availability

Data will be made available on request.

Received: 26 August 2025; Accepted: 18 December 2025;

References

1. Fantuzzi, L. & Cau, M. A. Investigating the provenance of the Baetican amphorae Dressel 23: New archaeometric evidence from Late Roman consumption centres. *Mediterr. Archaeol. Archaeom.* **17**, 47–68, https://doi.org/10.5281/zenodo.258085 (2017).
2. Vargas E.G. Amphora contents as commodities: the structure and function of tituli picti in the western Mediterranean in the 1st century AD, in: *Roman Amphora Contents: Reflecting on the Maritime Trade of Foodstuffs in Antiquity (In honour of Miguel Beltrán Lloris)*. Proceedings of the Roman Amphora Contents International Interactive Conference (RACIIC), Cádiz, 5–7 October 2015. Archaeopress Publishing Ltd, Oxford (2021) 51–62.
3. Pailler, J.-M. *Bolsena 1970. La maison aux peintures, les niveaux inférieurs et le complexe souterrain* (in French). *Bolsena 1970. The house with paintings, the lower levels and the underground complex*. Mélanges de l'École Française de Rome 83 (1971) 367–403.
4. Alemanno, V. et al. Analysis of Roman Era archaeological finds from Museo Territoriale del Lago di Bolsena with non-destructive investigation techniques. *IMEKO TC4 Int. Conf. Metrol. Archaeol. Cult. Herit.* **2023**, 43–48, https://doi.org/10.21014/tc4-arc-2023.009 (2023).

5. Gliozzo, E. Ceramic technology. How to reconstruct the firing process. *Archaeol. Anthropol. Sci.* **12**, 260, https://doi.org/10.1007/s12520-020-01133-y (2020).
6. Kazakou, T., Zorba, T., Vourlias, G., Pavlidou, E. & Chrissafis, K. Combined studies for the determination of the composition and the firing temperature of ancient and contemporary ceramic artefacts. *Thermochim. Acta* **682**, 178412, https://doi.org/10.1016/j.tca.2019.178412 (2019).
7. De Vito, C., Medeghini, L., Mignardi, S., Ballirano, P. & Peyronel, L. Technological fingerprints of the Early Bronze Age clay figurines from Tell Mardikh-Ebla (Syria). *J. Eur. Ceram. Soc.* **35**, 3743–3754, https://doi.org/10.1016/j.jeurceramsoc.2015.06.009 (2015).
8. Thér, R. et al. How was Neolithic pottery fired? An exploration of the effects of firing dynamics on ceramic products. *J. Archaeol. Method Theory* **26**, 1143–1175, https://doi.org/10.1007/s10816-018-9407-x (2019).
9. Maritan, L. Archaeo-ceramic 2.0: investigating ancient ceramics using modern technological approaches. *Archaeol. Anthropol. Sci.* **11**, 5085–5093, https://doi.org/10.1007/s12520-019-00927-z (2019).
10. Zhang, B. et al. Correlation study on firing temperature and color of plain pottery excavated from the Tang Dynasty tomb of Liu Jing in Shaanxi, China. *Herit. Sci.* **12**, 61. https://doi.org/10.1186/s40494-024-01178-5 (2024).
11. Kramar, S. et al. Mineralogical and geochemical characteristics of Roman pottery from an archaeological site near Mošnje (Slovenia). *Appl Clay Sci.* **57**, 39–48, https://doi.org/10.1016/j.clay.2011.12.008 (2012).
12. Viani, A., Sotiriadis, K., Len, A., Šašek, P. & Ševčík, R. Assessment of firing conditions in old fired-clay bricks: the contribution of X-ray powder diffraction with the Rietveld method and small-angle neutron scattering. *Mater. Charact.* **116**, 33–43, https://doi.org/10.1016/j.matchar.2016.04.003 (2016).
13. Fantuzzi, L., Ontiveros, M. A. C. & Macias, J. M. Amphorae from the Late Antique city of Tarraco-Tarracona (Catalonia, Spain): archaeometric characterization. *Periodico Di Mineral.* **84**, 169–212, https://doi.org/10.2451/2015PM0010 (2015).
14. Bernabale, M. et al. 3D fractures analysis and conservation assessment of wrought iron javelin through advanced non-invasive techniques. *Sci. Rep.* **13**(10142), 1–11, https://doi.org/10.1038/s41598-023-37179-w (2023).
15. Bernabale, M. et al. Correlative microscopy and Micro-Raman spectroscopy for enhancing the evaluation of corrosion damage in archaeological objects. *J. Cult. Herit.* **67**, 500–511, https://doi.org/10.1016/j.culher.2024.04.016 (2024).
16. Bernabale, M. et al. Correlative analysis of advanced microscopy techniques for metallography and corrosion microstructures of bronze Phoenician coins. *Mater. Charact.* **217**, 114441. https://doi.org/10.1016/j.matchar.2024.114441 (2024).
17. Coli, V. L. et al. Micro-computed tomography for discriminating between different forming techniques in ancient pottery: new segmentation method and pore distribution recognition. *Archaeometry* **63**, 1191–1210, https://doi.org/10.1111/arcm.12693 (2021).
18. Bernabale, M. et al. A comprehensive strategy for exploring corrosion in iron-based artefacts through advanced multiscale X-ray microscopy. *Sci. Rep.* **12**, 1–9, https://doi.org/10.1038/s41598-022-10151-w (2022).
19. Bernabale, M. et al. 3D imaging of micro-segregation and corrosion behavior of alloying elements in archaeological artefacts from Motya (Sicily, Italy). *Corros. Sci.* **211**, 110900. https://doi.org/10.1016/j.corsci.2022.110900 (2023).
20. Bernabale, M., Cognigni, F., Nigro, L., Rossi, M. & De Vito, C. Conventional and advanced techniques for archaeological diagnostic of iron artefacts. In: Proceedings of the IMEKO TC-4 International Conference on Metrology for Archaeology and Cultural Heritage, MetroArchaeo 2022, 2023: pp. 510–515.
21. Gait, J. et al. Novel application of SANS provides quantitative non-destructive identification of forming techniques in late Roman and early medieval pottery from Pannonia. *Sci. Rep.* **14**, 25926. https://doi.org/10.1038/s41598-024-77426-2 (2024).
22. Gait, J. et al. Quantitative 3D orientation analysis of particles and voids to differentiate hand-built pottery forming techniques using X-ray microtomography and neutron tomography. *Archaeol. Anthropol. Sci.* **14**, 1–18, https://doi.org/10.1007/s12520-022-01688-y (2022).
23. Caloi, I. & Bernardini, F. Revealing primary forming techniques in wheel-made ceramics with X-ray microCT. *J. Archaeol. Sci.* **169**, 106025. https://doi.org/10.1016/j.jas.2024.106025 (2024).
24. Kozatsas, J., Kotsakis, K., Sagris, D. & David, K. Inside out: assessing pottery forming techniques with micro-CT scanning. An example from Middle Neolithic Thessaly. *J. Archaeol. Sci.* **100**, 102–119, https://doi.org/10.1016/j.jas.2018.10.007 (2018).
25. Berg, I. X-radiography of Knossian Bronze age Vessels: assessing our knowledge of primary forming techniques. *Annu. Br. Sch. Athens* **104**, 137–173, https://doi.org/10.1017/S0068245400000228 (2009).
26. Andaloro, E., Belfiore, C. M., De Francesco, A. M., Jacobsen, J. K. & Mittica, G. P. A preliminary archaeometric study of pottery remains from the archaeological site of Timpone della Motta, in the Sibaritide area (Calabria—southern Italy). *Appl Clay Sci.* **53**, 445–453, https://doi.org/10.1016/j.clay.2010.07.021 (2011).
27. Medeghini, L. et al. The key role of micro-Raman spectroscopy in the study of ancient pottery: the case of pre-classical Jordanian ceramics from the archaeological site of Khirbet al-Batraway. *Eur. J. Miner.* **25**, 881–893, https://doi.org/10.1127/0935-1221/2013/0025-2332 (2014).
28. *Corpus Inscriptiorum Latinarum* (in Latin). *Corpus of Latin Inscriptions*. Vol. I, p. 3603.
29. Pailler, J. M. Bolsena. La maison aux peintures, les niveaux inférieurs et le complexe souterrain (in French). Bolsena 1970. The house with paintings, the lower levels and the underground complex. Mélanges de l'École Française de Rome 83-2 402–403 (1971).
30. Mauget, P. *La population et la société de la cité de Volsinii (Bolsena) (IIIe s. av. J.-C. – Ve s. ap. J.-C.)* (PhD thesis, in French). *The population and society of the city of Volsinii (Bolsena) (3rd century BC – 5th century AD)*, p. 781, n. 711.
31. Benelli, E. Rivista di Epigrafia Etrusca, in *Studi Etruschi* 59 (1993 [1994]) 292–293, n. 43 (in Italian).
32. *Corpus Inscriptiorum Latinarum* (in Latin). *Corpus of Latin Inscriptions*. Vol. I, p. 2929.
33. Corpus Inscriptiorum Latinarum (in Latin). Corpus of Latin Inscriptions. Vol. XI, p. 8117, 1.
34. Rigato, D. & Mongardi, M. Tituli picti con datazione consolare su anfore vinarie italiche: indagini preliminari (in Italian). *Tituli picti with consular dating on Italic wine amphorae: preliminary investigations*. In: M. Buora, S. Magnani (eds), *Le iscrizioni con funzione didascalico-esplicativa. Committente, destinatario, contenuto e descrizione dell'oggetto nell'instrumentum inscriptum* (in Italian). *Inscriptions with didactic-explanatory function. Client, recipient, content and description of the object in the instrumentum inscriptum*. Atti del VI incontro *Instrumenta Inscripta*, Aquileia (26–28 March 2015), *Antichità Altoadriatiche* LXXXIII. 103, 108 (2016).
35. Solé, V. A., Papillon, E., Cotte, M., Walter, P. & Susini, J. A multiplatform code for the analysis of energy-dispersive X-ray fluorescence spectra. *Spectrochim. Acta Part B Spectrosc.* **62**, 63–68, https://doi.org/10.1016/j.sab.2006.12.002 (2007).
36. Sanger, M. C. Investigating pottery vessel manufacturing techniques using radiographic imaging and computed tomography: Studies from the Late Archaic American Southeast. *J. Archaeol. Sci.: Rep.* **9**, 586–598, https://doi.org/10.1016/j.jasrep.2016.08.005 (2016).
37. Thér, R. & Toms, P. Orientation patterns characteristic for the structure of the ceramic body of wheel-thrown pottery. *Interdiscip.*

Archaeol. **12**, 143–154, https://doi.org/10.24916/iansa.2021.2.3 (2021).

38. De Vito, C., Medeghini, L., Mignardi, S., Coletti, F. & Contino, A. Roman glazed inkwells from the "Nuovo Mercato di Testaccio" (Rome, Italy): Production technology. *J. Eur. Ceram. Soc.* **37**, 1779–1788 (2017).
39. Ballirano, P. et al. A combined use of optical microscopy, X-ray powder diffraction and micro-Raman spectroscopy for the characterization of ancient ceramic from Ebla (Syria). *Ceram. Int.* **40**, 16409–16419 (2014).
40. Rathossi, C. & Pontikes, Y. Effect of firing temperature and atmosphere on ceramics made of NW Peloponnese clay sediments. Part I: Reaction paths, crystalline phases, microstructure and colour. *J. Eur. Ceram. Soc.* **30**, 1841–1851 (2010).
41. Cheilakou, E., Troullinos, M. & Koui, M. Identification of pigments on Byzantine wall paintings from Crete (14th century AD) using non-invasive Fiber Optics Diffuse Reflectance Spectroscopy (FORS). *J. Archaeol. Sci.* **41**, 541–555 (2014).
42. Nodari, L., Marcuz, E., Maritan, L., Mazzoli, C. & Russo, U. Hematite nucleation and growth in the firing of carbonate-rich clay for pottery production. *J. Eur. Ceram. Soc.* **27**, 4665–4673 (2007).
43. Bernabale, M. et al. Characterization of ultramarine blue in Roman wall paintings: case study from Volsinii (Bolsena, Italy). *Anal. Bioanal. Chem.* **417**, 1557–1566 (2025).

Acknowledgements

The authors acknowledge the financial support of Regione Lazio through the program DTC-Intervento TE1 (RSI project no. 305-2020-35585).

Author contributions

Martina Bernabale: Conceptualization, Writing – original draft, Methodology, Investigation, Formal analysis. Luca Buccini: Investigation, Formal analysis, Reviewing and editing. Pierfrancesco Atanasio: Investigation, Formal analysis, Reviewing and editing. Alessia Sanna: Investigation, Formal analysis, Reviewing and editing. Anna Candida Felici: Investigation, Formal analysis, Reviewing and editing, Supervision. Daniele Passeri: Reviewing and editing, Marco Rossi: Supervision, Resources, Reviewing and editing. Paolo Binaco: Conceptualization, Contribution to the historical and archaeological context. Danilo Dini: Conceptualization, Project coordination (REMEDIAVI), Supervision, Methodology. All authors read and approved the final manuscript.

Ethics approval, source of biological material, statement on animal welfare

Not applicable to this study.

Competing interests

The authors declare no competing interests.

Additional information

Supplementary information The online version contains supplementary material available at https://doi.org/10.1038/s40494-025-02279-5.

Correspondence and requests for materials should be addressed to Danilo Dini.

Reprints and permissions information is available at http://www.nature.com/reprints